Journal of Alloys and Compounds 995 (2024) 174799

Contents lists available at ScienceDirect

Journal of Alloys and Compounds

journal homepage: www.elsevier.com/locate/jalcom

Cost-effective synthesis of stable Co_xC@few-layered graphene nanostructures embedded in a carbon matrix

Carmen del Pino-Batlles [a,b], Aída Serrano [a], Alberto Castellano-Soria [b,c], Rosalía López-Méndez [d], Elena Navarro [b,c], Pilar Marín [b,c], Ana Espinosa [d,e], Noemí Carmona [b,c,*], Jesús López-Sánchez [a,**]

[a] Departamento de Electrocerámica, Instituto de Cerámica y Vidrio (ICV–CSIC), Madrid 28049, Spain
[b] Departamento de Física de Materiales, Facultad de Ciencias Físicas, Universidad Complutense de Madrid (UCM), Madrid 28040, Spain
[c] Instituto de Magnetismo Aplicado (IMA-UCM-ADIF), Madrid 28230, Spain
[d] IMDEA Nanociencia, c/ Faraday, 9, Madrid 28049, Spain
[e] Instituto de Ciencia de Materiales de Madrid (ICMM-CSIC), Madrid 28049, Spain

ARTICLE INFO

Keywords:
Sol-gel synthesis
Two-step surfactant strategy
Co-based core@shell nanostructures
X-ray absorption spectroscopy
Magnetic properties
Particle size confinement

ABSTRACT

In this study, a two-step surfactant sol-gel strategy is developed to synthesize Co particles with confined sizes in the nanoscale using organic precursors. This approach does not require the use of vacuum techniques or strong reducing atmospheres, making it a simple approach economically attractive. The strategy involves the generation of few-layered graphene shells to provide chemical stability, prevent oxidation and aggregation tendencies. Additionally, the study investigates the use of precursors based on nitrates and acetates, exploring their structural and magnetic properties in densified samples. Remarkably, magnetic properties are competitive for both approaches, with coercivities reaching up to 300 Oe and saturation magnetization of ~60 and ~80 emu/g for samples based on nitrates and acetates prepared at 650 °C, respectively. However, it is observed that smaller and more uniformly sized nanoparticles (around ~10 nm) are obtained with nitrate-based precursors due to an effective ligand decomposition process. Therefore, this chemical approach offers effective nanoscale confinement with intriguing magnetic properties through a cost-effective and reproducible synthesis.

1. Introduction

Cobalt (Co) nanoparticles hold great promise among metallic nanoparticles, capturing the attention of the researchers across diverse disciplines. Their appeal extends particularly to spintronic applications, where their magnetic properties, characterized by high saturation magnetization and significant uniaxial magnetic anisotropy [1–3], make them useful for high-density information storage and permanent magnets applications [4]. However, the attractiveness of Co nanoparticles extends beyond their magnetic properties, showing exceptional structural, electronic, and catalytic properties [3]. This versatility propels them into advanced applications, including biosensing of neurotransmitters (dopamine, DA) [5], cytotoxicity behavior and biocompatibility [6], high performance of Lithium-Sulfur [7] and Lithium-Selenium batteries [8], efficient hydrogen production [9,10], high-frequency electromagnetic absorbers [11], Fenton-like processes for organic wastewater treatments [12], stable oxygen reduction reactions [13,14], and sustainable bioelectricity generation in microbial fuel cells [15]. Consequently, the expansive scope of multidisciplinary applications underscores the fundamental role of Co nanoparticles in technological advancement and the resolution of challenges across diverse domains.

Although significant progress has been made in the confinement of Co particle sizes smaller than 20 nm [16–19], there is a concern in terms of their fabrication methods and their high tendency for aggregation. Regarding fabrication methods, the Co nanoparticles are obtained by microemulsion, typically requiring strong reducing conditions (i.e. hydrogen atmospheres) [18], or ultra-high vacuum conditions by ion implantation [17] and atomic layer deposition [19]. The high tendency to aggregate is because the metallic particles experience strong Van der Waals interactions which, together with magnetic dipole interactions, make it difficult to stabilize and disperse them [3,6]. Moreover, there is an added difficulty for possible targeted applications since Co

* Corresponding author at: Departamento de Física de Materiales, Facultad de Ciencias Físicas, Universidad Complutense de Madrid (UCM), Madrid 28040, Spain.
** Corresponding author.
E-mail addresses: ncarmona@ucm.es (N. Carmona), jesus.lopez@csic.es (J. López-Sánchez).

https://doi.org/10.1016/j.jallcom.2024.174799
Received 11 March 2024; Received in revised form 6 May 2024; Accepted 9 May 2024
Available online 11 May 2024

nanoparticles possess a special vulnerability to partially oxidize under ambient conditions, devaluating their high net magnetization [19]. All these complexities have led to the necessity of establishing both novel physical and chemical strategies that can actually be applied to their large-scale, reproducible, cost-effective, and chemically stable production.

Interesting routes are proposed by using a silica matrix in Co-based composites to confine particle sizes in the nanoscale [20,21]. Another effective method is the development of carbon-based core/shell structures [22–24] since a carbon shell provides high stability and good conductivity [25]. Complementary, it also offers the possibility of varying the functional groups, opening up a wide range of technological applications [26–30]. Therefore, the synergy between carbon and Co-based composites emerges to overcome the above-mentioned difficulties. Interestingly, Co@C core-shell nanoparticles are recently investigated for various purposes, mainly as a catalyst for oxygen reduction reaction [31–34], hydrogen generation [35] and syngas reaction [36], but also as a possible catalyst in solvents [37], microwave absorption enhancement [38], and/or for hyperthermia biomedical treatments [39].

In this work, we present a novel sol-gel route based on a two-step surfactant strategy for the synthesis of Co@few-layered graphene-based nanostructures embedded in a carbon matrix. The sol-gel technique provides high versatility in the use of precursors, the morphology can be controlled with relatively sharp size distributions, it is cost-effective, and chemical reactions can take place at room temperature [40–43]. Therefore, these characteristics provide a competitive advantage over other production methods such as chemical vapor deposition [44] and detonation technique [45], which require high vacuum instrumental conditions. The two-step surfactant strategy involves combining two complexing agents to directly target the precursor micelles of the Co nanoparticles. This ensures their chemical stabilization and provides the required carbon source for the ligand decomposition process, including polymerization and graphitization [46,47]. With this, a shell of few-layered graphene is generated that chemically shields the Co core, as observed in similar systems [46,47]. Following the two-step surfactant strategy, interesting works are carried out combining commonly oleylamine and oleic acid. Their combined action has been demonstrated to form this type of nanostructures, controlling their morphology and size by varying the ratios of their concentrations [48]. By contrast, we employ D-sorbitol as a complexing agent because it is biologically non-toxic, environmentally friendly, and low cost. Moreover, it possesses a great ability to react with the precursor micelles of Co nanoparticles since narrow particle size distributions of a few nanometers are obtained, acting as a crystal growth inhibiting agent. It can even reach complete inhibition of the crystal growth, with no particle formation under specific concentrations [49]. Therefore, it may be indispensable for particle size confinement at the nanoscale.

Subsequently, dodecylamine is chosen since it acts as a reducing agent with a high boiling point. There are interesting studies in which the use of dodecylamine mitigates the excessive formation of residual carbon since it is a saturated amine. Therefore, the contribution of carbon matrix would be reduced in comparison with other amines such as oleylamine [46]. Through this approach, we achieve Co@few-layered graphene-based nanostructures with chemically stable nanoparticle size distributions, with a mode below 10 nm. These structures exhibit interesting structural and magnetic properties, which vary depending on the chosen Co precursor (acetate or nitrate). The hydrolysis and polycondensation processes occur at room temperature and the densification process is carried out in a nitrogen atmosphere below 650 °C, which is sufficient for the carbothermal reduction process [50]. Consequently, the use of a polyol (D-sorbitol) and an amine (dodecylamine), following a two-step surfactant sol-gel strategy, proves to be an effective method to obtain Co@few-layered graphene-based nanostructures with attractive particle sizes for advanced catalytic and biomedical applications, among others, avoiding the use of vacuum techniques and/or highly reducing atmospheres.

2. Experimental methods

2.1. Sol-gel synthesis of Co@few-layered graphene nanostructures

The nanostructures are synthesized via sol-gel method employing a two-step surfactant strategy, utilizing the polyol D-sorbitol and the amine dodecylamine. These complexing agents possess high but slightly different melting points. Specifically, D-sorbitol melts at 296 °C while dodecylamine at 259 °C. This leads to a gradual decomposition of the organic surfactants during the densification process. Similarly, two Co precursors with distinct melting points are assessed: cobalt(II) nitrate hexahydrate (Sigma Aldrich, 98 %) with a melting point of ~56 °C, and cobalt(III) acetylacetonate (Sigma Aldrich, 98 %) with a melting point of 216 °C [51]. The significant thermal decomposition variation between precursors could play a pivotal role in facilitating proper intermixing of the added compounds, thereby promoting size confinement of Co@few-layered graphene nanostructures at the nanoscale.

The followed synthetic route is depicted in Fig. 1, illustrating the sequence of steps. First of all, we proceed to elaborate three dilutions:

a) Cobalt solution: Co salt precursor solution is dissolved in absolute ethanol (EtOH) (CH_3CH_2OH, Panreac) with a molar ratio respectively 1:8 (1).
b) D-sorbitol solution: D-sorbitol ($C_6H_{14}O_6$, Sigma Aldrich, 99 %) is dissolved in deionized water with a molar ratio of 1:30. D-sorbitol serves as a crystal growth inhibitor by providing essential hydroxyl groups for forming complex systems. This action prevents rapid hydrolysis and polycondensation, thereby promoting the formation of fine particles [49].
c) Dodecylamine solution: Dodecylamine ($CH_3(CH_2)_{10}CH_2NH_2$, Sigma Aldrich, 98 %) is dissolved in absolute EtOH with a molar ratio 1:30. Dodecylamine is incorporated in the same ratio as a steric and reducing agent, contributing to an alkaline pH.

In turn, molar ratio between the Co precursor and the D-sorbitol or dodecylamine solutions is 1:10. For clarity, the molar ratios used for the solutions are also listed in Table 1:

The three solutions undergo magnetic stirring for chemical homogenization for 20 minutes. Subsequently, the D-sorbitol solution is added dropwise into the Cobalt solution (2). After another 20 minutes, the Dodecylamine solution (3) is also added dropwise. The resulting solution is kept under magnetic stirring for 1 day (4). Then, the temperature is raised to 80 °C to evaporate the remaining EtOH and maintained for an additional 2 days (drying step, 5), obtaining the xerogels. It is important to note that Co nitrate undergoes transformation into Co oxide starting from 74 °C in air [51]. Conversely, when Co precursor micelles are utilized with acetates as precursors, oxide formation occurs at higher temperatures, as observed in recent studies [52]. The densification process is conducted under a nitrogen flow (99.8 %) ranging between 20 and 50 cm^3/min in a horizontal tube furnace (6). The heating ramp is set at 5 °C/min until reaching temperatures between 450 and 650 °C for 1 hour. This thermal window is consistent with similar systems used to address the carbothermal reduction process to form the desired nanostructures [47,52]. Subsequently, a cooling rate of 10 °C/min is employed until reaching room temperature (7). Finally, the sample is ground in an agate mortar until a fine and homogeneous powder is obtained (8).

2.2. Structural and magnetic characterization

Composition and crystal structure were studied by X-ray diffraction (XRD) using a Bruker D8 diffractometer Cu K_α radiation ($\lambda = 1.5418$ Å) with a Lynxeye XE-T detector. Subsequently, Rietveld refinements of the XRD patterns for obtain the crystal structure, lattice parameters,

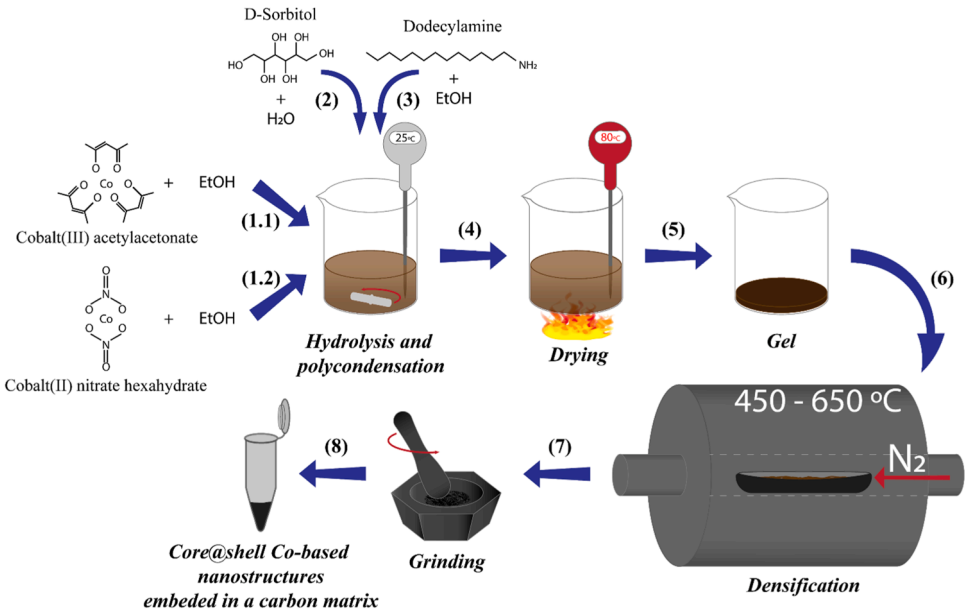

Fig. 1. Schematic route for the synthesis of Co-based nanostructures by sol-gel. (1) Co salt precursor based on nitrate and acetate is dissolved in ethanol absolute. (2) D-sorbitol and (3) dodecylamine are subsequently incorporated dropwise into the solution. (4) Chemical homogenization for 1 day. (5) Drying step at 80 °C for 2 days. (6) Densification process between 450 and 650 °C. (7) Grinding step in an agate mortar. (8) Resulting core@shell Co-based nanostructures.

Table 1
Constituent molar ratio related to the prepared solutions for the sol-gel synthesis.

Solutions	Constituent molar ratio
Cobalt solution	(i) Cobalt (II) nitrate hexahydrate: EtOH = 1: 8 (ii) Cobalt(III) acetylacetonate: EtOH = 1: 8
D-sorbitol solution	D-sorbitol: H_2O = 1: 30
Dodecylamine solution	Dodecylamine: EtOH = 1: 30

compositional percentage of phases, and volume-weighted average sizes, were performed using the Profex interface of the BGMN software [53]. In addition, the Co valence and a short-order structural range characterization of the Co-based nanostructures were carried out by X-ray absorption spectroscopy (XAS). XAS experiments were carried out at the CLÆSS-BL22 beamline of the ALBA synchrotron facility in Cerdanyola del Vallès (Spain) [54]. Both X-ray absorption near-edge structure (XANES) and extended X-ray absorption fine structure (EXAFS) measurements were performed at the Co K-edge (7709 eV) at room temperature. Metal Co foil was measured and used to calibrate the energy. Samples and CoO and Co_3O_4 references in powder form were mixed with cellulose and pressed into pellets to be measured in transmission configuration. The monochromator used was a double Si crystal oriented in the (311) direction. The XAS analysis was carried out using the Athena and Artemis software [55,56]. The modulus of the Fourier transform (FT) of the EXAFS signal at the Co K-edge was performed in the k^2 $\chi(k)$ weighted EXAFS signal between 2.5 and 11 $Å^{-1}$. Experimental EXAFS results were fitted in R-space in the range 1.2–3.0 Å using the FEFFIT code [55,56]. The fitting was performed by fixing the shift at the edge energy E_0 and using the number coordination N, the interatomic distance R and the Debye-Waller (DW) factors as free parameters. Complementary, structural properties and particle size distribution were also examined with a high-resolution transmission electron microscopy (TEM) JEM-3000 F. TEM images were analyzed by the ImageJ software.

Magnetic properties of the nanostructures were investigated with a vibrating sample magnetometer (VSM) attached to a physical property measurement system (PPMS model 6000 controller, Quantum Design). Magnetic hysteresis loops were collected at room temperature with a maximum applied magnetic field of 50 kOe.

3. Results and discussion

The XRD patterns of samples prepared at 450, 600, and 650 °C using nitrate and acetate as Co precursors are presented in Fig. 2a. Overall, there is a remarkable contrast between the compounds formed at 450 °C and those above 600 °C, regardless of the chosen precursor. Initially, at 450 °C, the emergence of cobalt monoxide (CoO) is evident, as indicated by diffraction peaks at approximately ~36.7, ~42.7, and ~61.7° [30]. The XRD reflections exhibit relatively broad peaks, indicating that the crystalline domain size is at the nanoscale.

This compound predominates in samples utilizing both precursors and it is accompanied by an extended shoulder around 26°, which is attributed to the contribution of amorphous carbon [28,57]. Upon increasing the temperature to 600 °C, a significant transformation occurs in the nature of the densified samples, with the predominant formation of metallic Co crystallizing in face-centered cubic (fcc) structure, evidenced by diffraction peaks around ~44.4, ~51.2, and ~76.0°, and hexagonal close-packed (hcp) structure, with diffraction peaks approximately at ~41.9, ~47.7, and ~76.0° [58,59]. Thermodynamically, the most energetically favourable crystal structure at room temperature is the hexagonal close-packed (Co_hcp) structure, while the face-centered cubic (Co_fcc) structure is favoured above 695 K. However, surface effects arising from nanometric scale suggest that both crystallizations may coexist at room temperature [58,60]. These results validate the sol-gel synthesis method for the formation of metallic Co, using friendlier and more cost-effective environments such as a nitrogen atmosphere.

As for the contribution of matrix carbon, no significant changes are observed with respect to the samples prepared at 450 °C. However, as the temperature rises to 650 °C, this contribution begins to magnify, showing an increase in relative intensity and narrowing width of the diffraction peaks. This phenomenon indicates evident ligand decomposition at 650 °C. Similar effects have been observed in other studies at comparable densification temperatures, where metallic particles serve as catalysts during the graphitization process [47,61]. Likewise, similar features are identified in the XRD peaks when examining the contribution related to metallic Co, both hcp and fcc structures. The sample

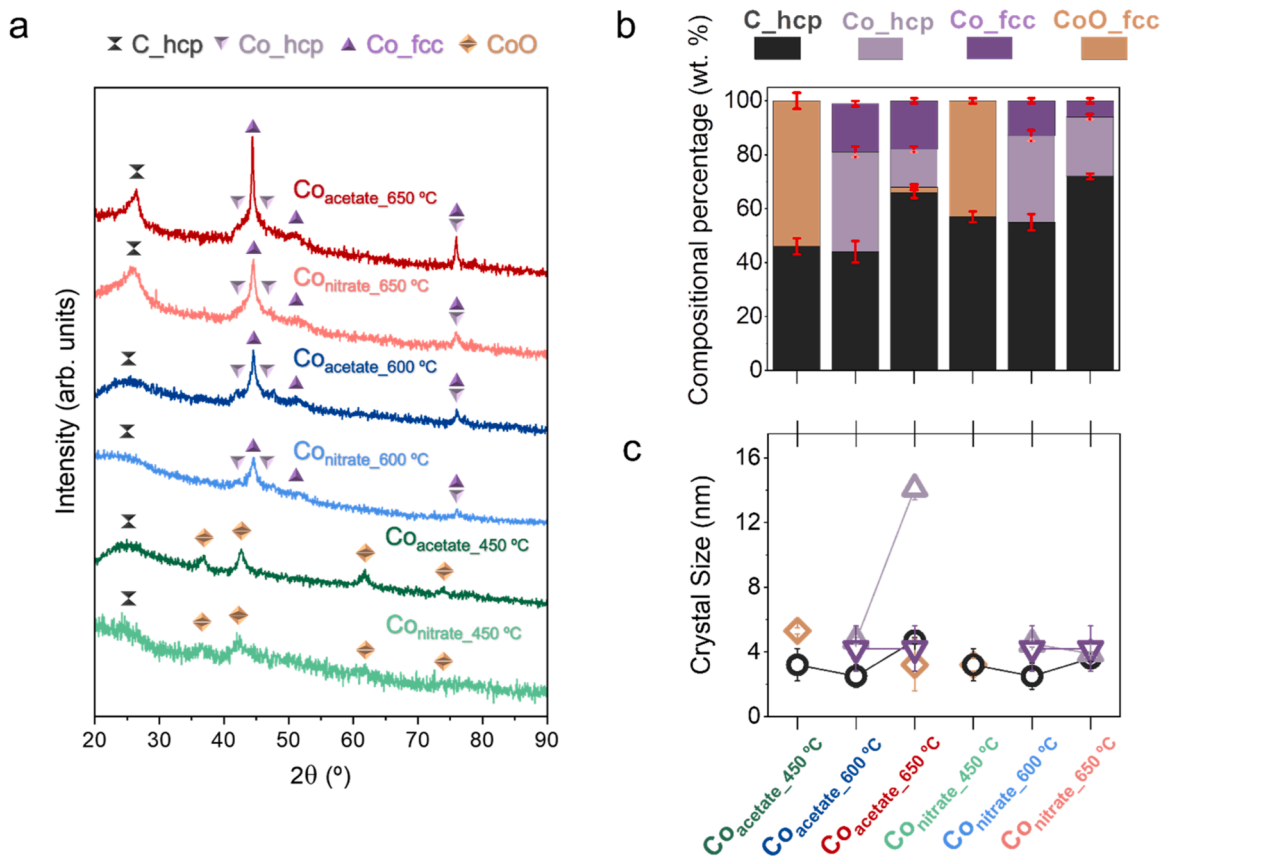

Fig. 2. (a) XRD spectra of the samples synthesised at 450, 600 and 650 °C using different Co precursors (nitrate and acetate). The characteristic XRD reflections of each phase are indicated in each pattern. (b) Compositional percentage and (c) crystal size of the Co-based samples calculated by Rietveld refinement.

prepared with acetate exhibits narrower widths of the diffraction peaks compared to those obtained using nitrate-based precursor. The effect is also observed at 600 °C, indicating a confinement of crystalline domain size to smaller dimensions, particularly in samples prepared with nitrate as precursor.

The structural parameters obtained through Rietveld analysis are presented in Fig. 2b, illustrating the percentage of phases, and Fig. 2c, displaying their corresponding crystal sizes. Beginning with the percentage phase composition, it is noticeable that the amount of crystalline carbon formed is higher in the nitrate-based samples compared to the acetate-based samples. This suggests that the ligand decomposition process is more effective when using nitrate. Furthermore, a notable increase of ~24 % and ~33 % is observed in the two sets of samples when the densification temperature is raised from 600 to 650°C for the nitrate and acetate-based samples, respectively. Hence, the process of ligand decomposition starts at lower temperatures and progresses gradually in nitrate-based samples. Concerning the Co-based compounds, no significant differences are observed for densification temperatures ranging between 450 and 600 °C. However, the ratio Co_fcc/Co_hcp is 3.67 in the case of nitrate and 0.78 in the case of acetate when densified at 650 °C. The change in crystalline phase tendency could be attributed to an increase in particle size in acetate-based samples, thereby promoting hcp crystallization [60]. Fig. 2c provides additional insights, indicating that while the crystalline domain size remains within the range of ~3–6 nm for all identified crystalline phases and densification temperatures considered, a noteworthy change is observed for Co_fcc in acetate-based sample prepared at 650 °C. Here, the crystalline domain size increases by ~3.5 times, reaching up to ~14 nm. Although this change may be considered small in absolute terms, it suggests that the effects of particle size confinement begin to diminish for the acetate-based samples produced at 650 °C.

The retrieved lattice parameters corresponding to the Co-based phases are tabulated in Table 2. Notably, the fcc structure of CoO exhibits variation in lattice parameter depending on the densification temperature and the precursor used. Specifically, a lattice parameter value of 4.26 Å has been reported [62]. Comparison with the values in Table 2 suggests either dilatation (a,$Co_{nitrate\_450\ °C}$) or compression (a, $Co_{acetate\_450\ °C}$) of its crystalline structure. However, drawing further conclusions is challenging at 450 °C due to potentially high organic matter content and the incipient nature of carbothermal reduction and ligand decomposition processes. At 600 °C, these processes become more pronounced, and the lattice parameters of the Co_fcc structure

Table 2
Retrieved lattice parameters calculated by Rietveld analyses related to Co-based compounds.

Sample	Compound / Crystal structure	Space group nº	a (Å)	c (Å)
$Co_{acetate\_650\ °C}$	CoO / fcc	225	4.223(7)	–
	Co / fcc	225	3.563(3)	–
	Co / hcp	194	2.511(3)	4.05 (7)
$Co_{nitrate\_650\ °C}$	Co / fcc	225	3.559(7)	–
	Co / hcp	194	2.516(6)	4.05 (7)
$Co_{acetate\_600\ °C}$	Co / fcc	225	3.549(6)	–
	Co / hcp	194	2.506(5)	4.05 (7)
$Co_{nitrate\_600\ °C}$	Co / fcc	225	3.554(6)	–
	Co / hcp	194	2.509(5)	4.05 (7)
$Co_{acetate\_450\ °C}$	CoO / fcc	225	4.26(2)	–
$Co_{nitrate\_450\ °C}$	CoO / fcc	225	4.270(7)	–

exhibit slightly higher values compared to those reported in other studies, typically around a = 3.544 Å and a = 3.543 Å [58,63]. Similar trends are observed for the lattice parameters of the Co_hcp structure, with typical values of a = 2.507 Å and c = 4.08 Å [58]. Interestingly, the slight dilation in the lattice parameters of metallic Co may be attributed to the incorporation of carbon into its crystalline structure, which could confer higher chemical stability against oxidation [64].

In order to corroborate those crystalline phases detected by XRD (Fig. 2) and evaluate the coordination and the short-range order of absorbing atoms, both XANES and EXAFS investigations are performed at the Co K-edge in the samples varying the precursor and their densification temperature. XANES spectra of samples along with those of Co foil, CoO and Co_3O_4 powder references are shown in Fig. 3a. Two sets of absorption signals are identified: an absorption signal close to that of the CoO reference for samples prepared at 450 °C and the other one similar to the absorption response of Co foil for the samples prepared at higher temperatures.

The first inflection point of the main Co K-absorption edge is associated with 1 s-4p transitions [65] and its energy position is displayed in Fig. 3(b) along with the energy position of the absorption edges for metallic Co foil, CoO and Co_3O_4 references. Comparing the energy position of the absorption edge for samples and references, the average oxidation state of the Co absorbing atom for all samples is calculated according to the Kunzl's law [66,67]. While for samples annealed at 450 °C shows an oxidation state similar to the CoO reference, samples densified at 600 and 650 °C exhibit a reduction of the Co-based compounds valence close to the metallic Co foil. In turn, slight variations in the energy position between the samples and the references can be related to changes in the coordination of Co absorbing atoms by the incorporation of C atoms into the Co-based structure. In the same way, variations at the whiteline for samples densified at 450 °C and after the absorption edge for samples prepared at 600 and 650 °C in the first resonances with respect to the references can be associated with the change of coordination of the samples. In addition, differences in the first resonances for samples prepared at 600 and 650 °C can be also attributed to the differences between the Co_hcp and Co_fcc structure [68], as is previously identified by XRD (Fig. 2).

Fig. 3c displays the modulus of the FT calculated from the EXAFS signal at the Co K-edge, alongside the Co foil and CoO reference. For the fitting, two shells produced by the interaction of a Co absorbing atom with O and Co atoms for samples prepared at 450 °C, and one shell from the interaction of a Co absorbing atom with Co atoms for samples prepared at higher temperatures, are considered. Table 3 presents the numerical EXAFS results obtained from the fitting for the samples, as well as the results for the references. The EXAFS signal of samples prepared at 450 °C exhibits one shell around 2.1 Å attributed to Co-O neighbour distances, and another shell at 3.0 Å related to Co-Co distances. The former falls at smaller distances than the CoO reference, while the Co-Co distance is similar. Additionally, a significant decrease in the whiteline intensity is observed for both samples, with a lower intensity for those prepared from nitrate-based samples. In both cases, a pre-edge peak is also identified at larger positions (1.3 eV), which is related to dipole forbidden transitions 1 s → 3d [69]. The pre-edge peak exhibits higher

Table 3
EXAFS parameters obtained at the Co K-absorption edge: N (coordination), R (radial distribution), and DW (Debye Waller factor) for the samples along with the Co foil and CoO reference.

Sample	Shell	N	R (Å)	DW (Å^2)
Co_foil	Co-Co	12	2.493(1)	0.0062(2)
$Co_{acetate\_650\ °C}$	Co-Co	7.8(1)	2.493(4)	0.007(1)
$Co_{nitrate\_650\ °C}$	Co-Co	9.1(2)	2.492(2)	0.007(1)
$Co_{acetate\_600\ °C}$	Co-Co	8.6(3)	2.490(3)	0.007(1)
$Co_{nitrate\_600\ °C}$	Co-Co	8.9(3)	2.489(3)	0.007(1)
$Co_{acetate\_450\ °C}$	Co-Co	8.9(1)	3.012(5)	0.012(2)
	Co-O	4.6(1)	2.083(8)	0.008(2)
$Co_{nitrate\_450\ °C}$	Co-Co	6.5(1)	3.005(5)	0.014(2)
	Co-O	4.4(2)	2.056(6)	0.010(2)
CoO_reference	Co-O	6	2.14(2)	0.012(5)
	Co-Co	12	3.006(4)	0.010(2)

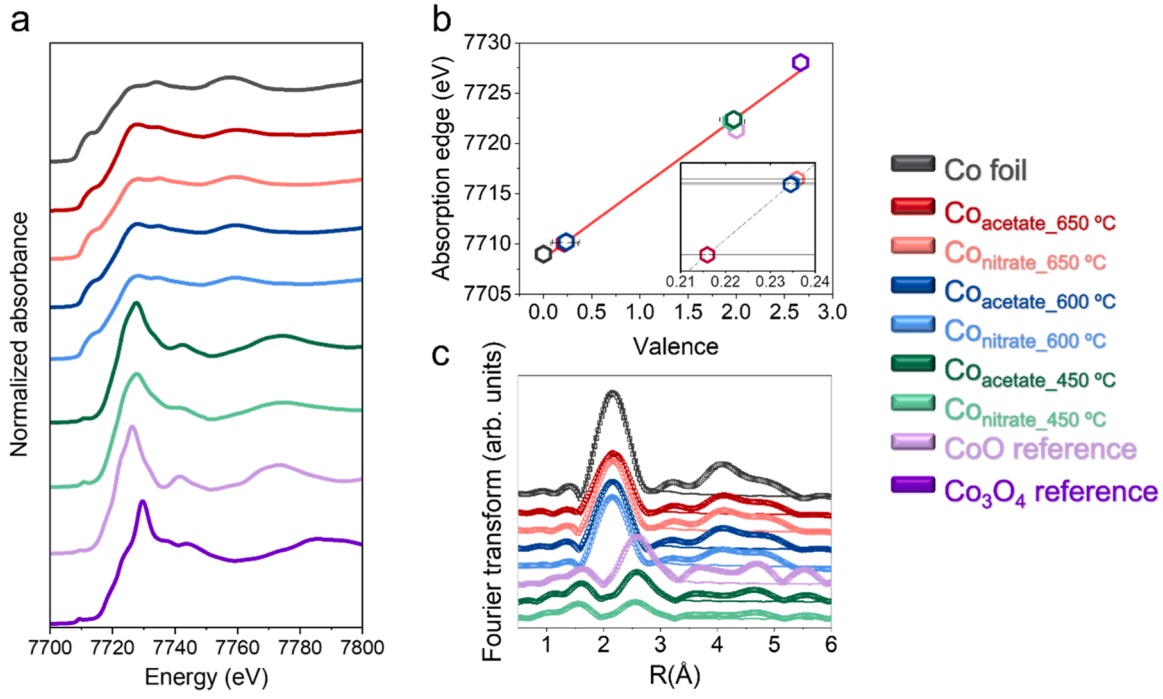

Fig. 3. (a) XANES spectra at the Co K-edge for the different samples together with the Co foil and CoO and Co_3O_4 references. (b) Average valence for the samples calculated from the position at the absorption edge in XANES region and the linear relationship obtained from the oxidation state and the position at the absorption edge of references (Co, CoO and Co_3O_4). (c) FT of EXAFS signal for Co foil, CoO reference and different samples along with the best-fitting simulations (continuous lines).

intensity than that of the CoO reference, suggesting a structural disorder in the environment of Co atoms, possibly transitioning to a more complex structure with atoms distributed in tetragonal symmetry [70]. This distortion in short-range order and the reduction in coordination number may be associated with the incorporation of carbon atoms into the CoO structure. For samples prepared at higher temperatures, a shell around 2.5 Å related to Co-Co distances is identified, which coincides with the position of metallic Co foil. Additionally, a decrease in coordination number is observed for all samples, particularly pronounced in the acetate-based sample prepared at 650 °C. This reduction could be attributed to a change in chemical coordination, such as the incorporation of carbon atoms into the Co structure, as suggested by XANES signal analysis. Regarding the Debye-Waller (DW) factor across all samples, no significant variations are noted compared to the respective references. These results collectively indicate the possible presence of carbon atoms within the Co-based structure of stabilized phases, with no additional amorphous phases detected beyond those observed by XRD (Fig. 2).

Next, we proceed to investigate the morphology, size and distribution of crystalline compounds within the carbon matrix through local TEM analyses (Fig. 4). The selected samples for analysis are those demonstrating a notable process of ligand decomposition and the formation of metallic Co, namely those densified at 600 and 650 °C. Fig. 4a, e depict representative TEM images corresponding to the acetate-based samples, while Fig. 4i,m illustrate those based on nitrate, prepared at 600 and 650 °C, respectively. In these images, Co nanoparticles embedded in a carbon matrix are discernible, with their sizes varying depending on the Co precursor used and the densification temperature. For a quantitative analysis, the particle size distribution is calculated, following a lognormal distribution function, which is typical of nanoparticles synthesized by the sol-gel method [71]. The average particle size ($d_{average}$) exhibits an increase with temperature, from 15.2(6) to

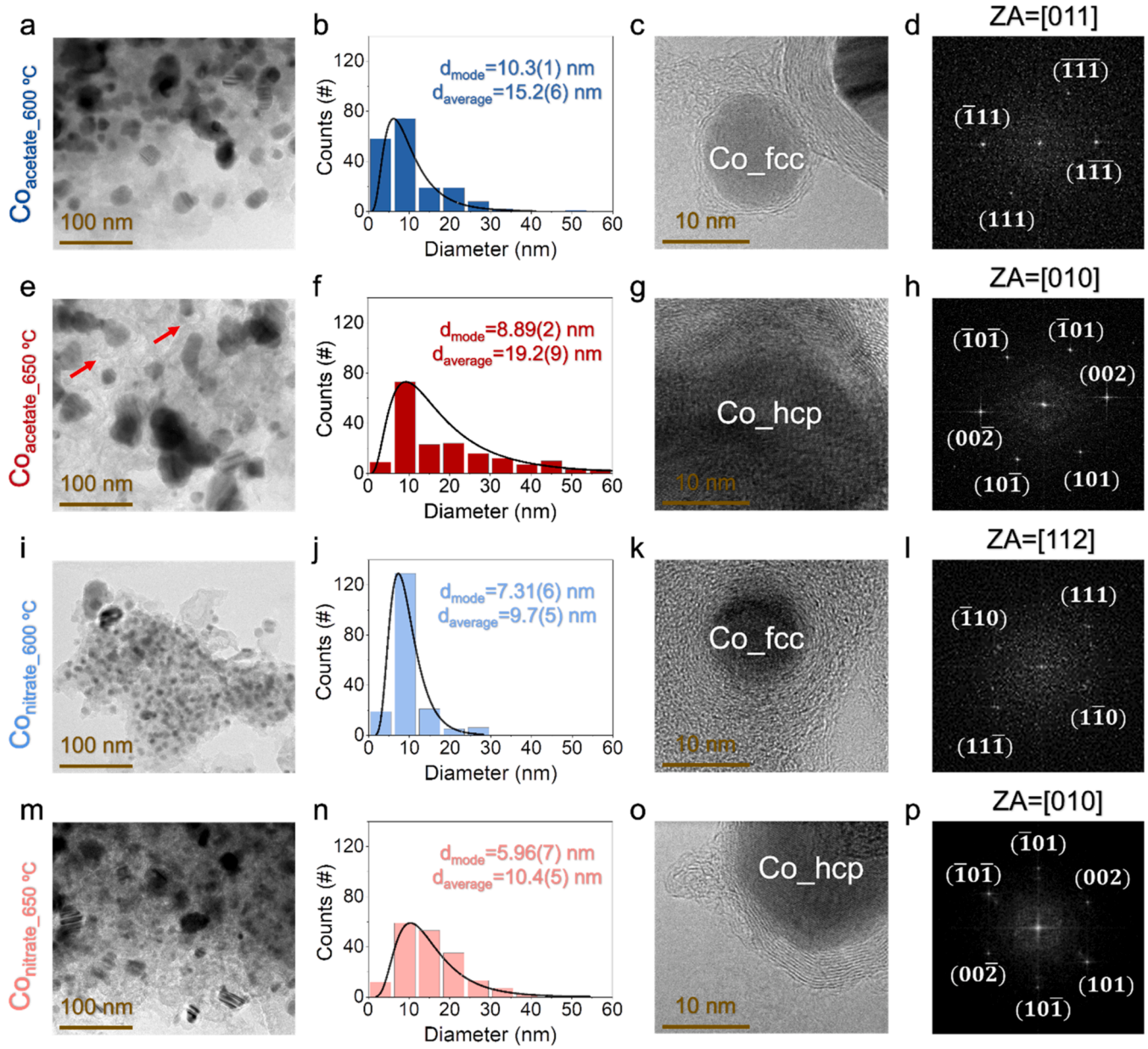

Fig. 4. Representative TEM images, particle size distribution, high-resolution TEM images, and FFT of the acetate-based samples prepared at (a-d) 600 and (e-h) 650 °C, and nitrated-based samples at (i-l) 600 and (m-p) 650 °C, respectively. Zone axis (ZA) is provided on top of the FFT figures. Red arrows indicate empty shells in Figure e. (For interpretation of the references to color in this figure legend, the reader is referred to the web version of this article.)

19.2(9) nm in the case of acetate-based samples, and from 9.7(5) to 10.4 (5) nm in the case of nitrate-based samples (Fig. 4b,f,j,m). Considering that the crystalline domain size obtained by Rietveld analyses ranges from ~4 to ~15 nm, we infer the co-existence of both single-crystal and polycrystalline particles, with the contribution of the latter increasing with temperature. This behavior is expected, as the degree of atomic diffusion tends to rise with temperature. However, analyzing in detail, the nitrate-based samples possess distribution modes (d_{mode}) of 7.3(2) and 6.2(1) nm respectively for 600 and 650 °C. Interestingly, the particle size ratio below ~10 nm is higher for the sample densified at 600 °C. Such effect could be due to the possible occurrence of non-stoichiometric oxygen and carbon incorporated in the crystal structure of metallic Co at 600 °C within the larger nanoparticles and as the process of carbothermal reduction and ligand decomposition is more effective at 650 °C, they are broken down into smaller size nanoparticles. In addition, the same effect could occur in the acetate-based samples since the mode of the distribution slightly decreases from 10.4(3) to 9.2(1) nm for 600 and 650 °C, respectively. Notably, the standard deviation of the distribution increases in the case of the nitrate-based samples, from 6.56(2) to 7.21(4) nm. However, in the case of the acetate-based samples, its standard deviation doubles, from 7.42 (6) to 14.73(8) nm. These results, taken together with the mode and standard deviation of the distribution, indicate that smaller particle sizes with narrower size distributions are obtained when using nitrate as the Co precursor. In contrast, acetate-based samples exhibit a significant fraction of particles above 20 nm. Therefore, the size confinement effects of a few tens of nanometers, with potential applicability in catalysis, are more effectively achieved using nitrate-based samples.

High-resolution TEM analyses are also conducted to examine the crystallization of Co nanoparticles and their close chemical environment in detail (Fig. 4c,g,k,o). These analyses reveal that the Co nanoparticles actually form a core@shell structure, with the shell being constituted by few-layered graphene, as evidenced by the interplanar distances of the shell, which are approximately ~3.6 Å [28,47]. Furthermore, a fast Fourier transform (FFT) analysis is performed to identify the interplanar distances of the oriented crystalline structures of the core (Fig. 4d,h,l,p). The crystallizations corresponding indistinctly to Co_hcp and Co_fcc nanoparticles are found, consistent with the previous determination carried out by XRD (Fig. 2). Overall, these compositional features indicate that the sol-gel strategy employed effectively passivates the Co nanoparticles against oxidation.

The acetate-based samples also exhibit empty shells, as indicated by the red arrows of Fig. 4e, suggesting an ejection of Co particles. This phenomenon could contribute to a higher degree of agglomeration, primarily due to magnetostatic interactions and/or an increase in particle size. This observation could elucidate the increase in the crystalline domain size observed in the Co_acetate_650 °C sample, as well as its wider standard deviation in distribution compared to the use of nitrate as a precursor. Consequently, while core@shell nanostructures are achieved using both precursors, those synthesized with nitrate could disperse more homogeneously, effectively spreading the Co nanoparticles and mitigating magnetic interactions between particles. The effect may be attributed to a higher percentage of carbon crystallization in the nitrate-based samples, as depicted in Fig. 2c.

The magnetic properties of Co-based nanostructures are investigated by VSM. Fig. 5a displays the hysteresis cycles obtained at room temperature, with a magnification of the central zone provided for each densification temperature: 450 °C (Fig. 5b), 600 °C (Fig. 5c), and 650 °C (Fig. 5d). It is important to note that the magnetization of the material is normalized, considering the percentage of cobalt-based phases obtained from Rietveld analysis, while excluding the crystalline contribution of

Table 4
Magnetic values nitrate- and acetate-based samples densified from 450 to 650 °C, retrieved from the magnetic hysteresis loops acquired at room temperature under a maximum applied magnetic field of 50 kOe.

Sample	M_S at 50 kOe (emu/g)	M_R (emu/g)	H_C (Oe)
$Co_{acetate\_650\ °C}$	82.4	17.1	300
$Co_{nitrate\_650\ °C}$	61.7	15.5	300
$Co_{acetate\_600\ °C}$	44.7	7.7	230
$Co_{nitrate\_600\ °C}$	60.7	0	0
$Co_{acetate\_450\ °C}$	2.5	0	0
$Co_{nitrate\_450\ °C}$	3.7	0	0

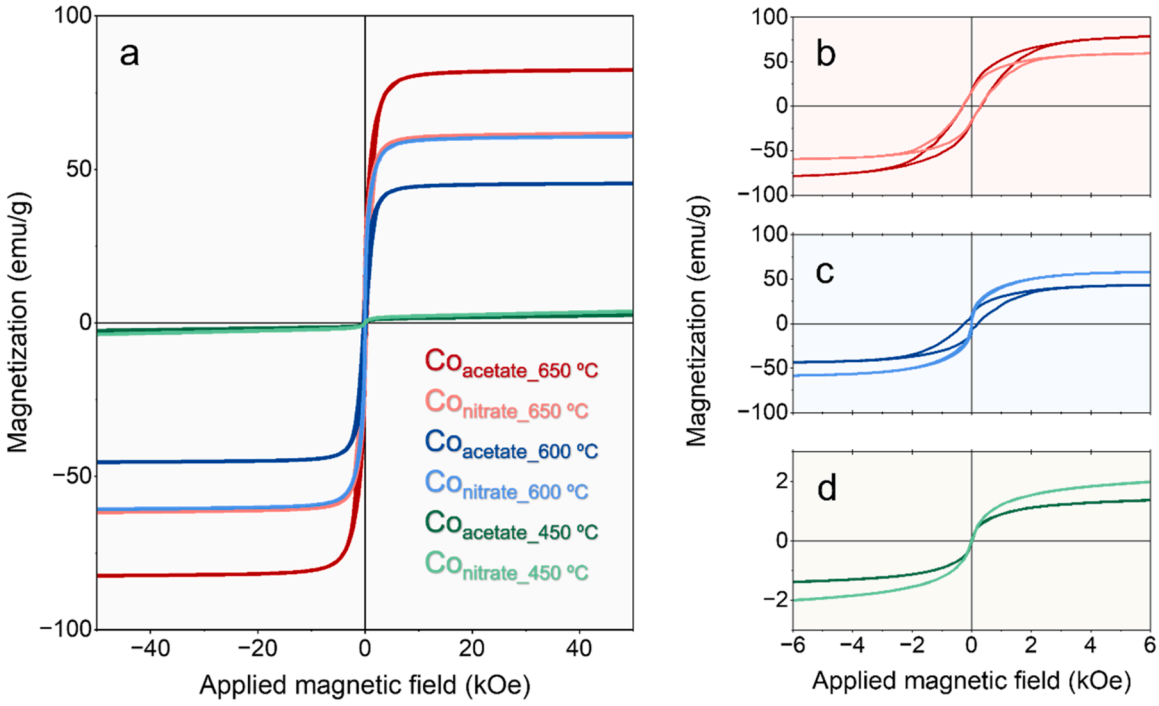

Fig. 5. (a) Magnetic hysteresis loops and (b-d) magnifications of the central area corresponding to the samples based on nitrate and acetate prepared at 450, 600 and 650 °C, respectively.

the carbon matrix. In this context, Table 4 shows the values of saturation magnetization (M_S), remanent magnetization (M_R), and coercive field (H_C) for all the samples. Notably, the magnetic properties of the samples exhibit a high dependency on purity and size control, resulting in significant differences. The samples synthesized at 450 °C exhibit a superparamagnetic hysteresis cycle at room temperature, with M_S values of 3.7 and 2.5 emu/g for the use of nitrate and acetate as the Co precursor, respectively. However, only CoO was detected at this temperature by XRD (Fig. 2), and this material displays paramagnetism at room temperature [72]. Therefore, it is highly probable that there is a small formation of Co nanoparticles at 450 °C, which may not be detectable by XRD and undiscernible by XANES signal, since the saturation magnetization of metallic Co is in the order of 160 emu/g [73]. Continuing with the samples prepared at 600 °C, the nitrate-based sample also exhibits a high superparamagnetic character, accompanied by a slight magnetically harder contribution (Fig. 5c). Superparamagnetism arises in single magnetic domain nanoparticles whose physical size is well below a critical size (25 $K_{ef}\ V_{SP} = K_b\ T$ where K_{ef} is the effective magnetic anisotropy, V_{SP} is the superparamagnetic critical volume, K_b is the Bolzman constant and T the absolute temperature). For metallic Co particles, this critical size is below 20 nm [74]. Therefore, this reasoning is supported by the average particle size of 9.7(5) nm and a distribution mode of 7.3(2) nm. Similarly, the acetate-based sample also exhibits superparamagnetic characteristics within the central region of the hysteresis cycle. However, the dominant contribution is ferromagnetic, marked by a certain coercivity (230 Oe), attributed to Co nanoparticles roughly larger than 20 nm. This observation aligns with the utilization of acetate as a precursor, which yields larger particles compared to nitrates at the same densification temperature (Fig. 4).

The samples prepared at 650 °C already display robust ferromagnetism using both precursors, with similar coercivities of 300 Oe. Initially, it is expected that the acetate-based sample could exhibit consolidated ferromagnetism, given its higher degree of agglomeration and particle size compared to the nitrate-based sample. However, the predominance of Co nanoparticles below 20 nm is evident in the nitrate-based sample. One plausible explanation could be that larger Co particles magnetically align neighboring smaller particles exhibiting ferromagnetism, and/or these smaller particles collectively behave as a larger particle when aggregated [75,76]. Comparing with other works, on the one hand, previous studies [38] demonstrate Co nanoparticles with crystallite sizes ranging from 10.2 to 29.5 nm, exhibiting ferromagnetic behavior and achieving M_S values of 28.5 and 78.0 emu/g, M_R of 6.25 and 22.5 emu/g, and H_C of 20 and 60 Oe, respectively. On the other hand, Sun et al. [21] synthesized Co nanoparticles with a particle size of 30 nm, resulting in M_S values of 37.39 emu/g, M_R of 2.06 emu/g, and H_C of 164 Oe [45]. In this study, relatively high magnetization values are attained for the samples synthesized at 600 and 650 °C, reaching maximum values of ~82.4 emu/g for the $Co_{acetate\_650\ °C\ sample}$. The difference in coercivities compared to those works may be interpreted as the effective incorporation of carbon in the metallic Co crystalline structure, as evidenced by XRD (Fig. 2) and XAS (Fig. 3). It is noteworthy that although the Co_fcc/Co_hcp ratio is different in the two precursors (3.67 in the case of nitrate and 0.78 in the case of acetate), the coercivity does not depend on crystalline anisotropy. This phenomenon could impede the reversal of magnetization when an external magnetic field is applied, increasing its coercivity. Furthermore, the M_S values are competitive with those found in those works [38,45], although there may be slight variations in the magnetization normalization with respect to carbon weight. This discrepancy could arise from a contribution of amorphous carbon that is not being accounted for the normalization. Nevertheless, these are interesting M_S and H_C values, and the nitrate-based sol-gel strategy offers significant passivation of the Co nanoparticle, forming a core@shell structure that stabilizes and confines its size to a few nanometers. Such a feature will prevent future degradation of its magnetic properties due to oxidation and will promote surface effects resulting from their nanoparticle sizes, with potential applicability for multidisciplinary purposes.

4. Summary and conclusions

Important sol-gel insights are addressed in this research regarding the obtaining of stable core@shell structures based on Co@few-layered graphene with confined sizes at the nanoscale. To achieve this, the two-step surfactant strategy is employed using D-sorbitol as an inhibitor of the growth of the precursor micelle of metallic Co and dodecylamine to stabilize it and provide the necessary amount of carbon for the formation of the shell and the carbon matrix through a process of polymerization and graphitization. A comprehensive structural and magnetic study is carried out on samples using nitrate and acetate as Co precursors, finding narrower size distributions, lower dispersion, and smaller sizes with the use of nitrate. Additionally, structural incorporation of C into the Co core is detected, potentially providing greater chemical stability. These results, combined with their interesting and competitive magnetic properties, make this system a powerful candidate for magnetic applications among others, offering an effective, simple, low-cost, and reproducible method for the synthesis of Co-based nanostructures passivated with few-layered graphene.

CRediT authorship contribution statement

Pilar Marín: Writing – review & editing, Investigation, Formal analysis, Data curation, Conceptualization. **Ana Espinosa:** Writing – review & editing, Resources, Investigation, Formal analysis, Data curation, Conceptualization. **Elena Navarro:** Writing – review & editing, Investigation, Formal analysis, Data curation, Conceptualization. **Noemí Carmona:** Writing – review & editing, Writing – original draft, Visualization, Validation, Supervision, Resources, Project administration, Methodology, Investigation, Funding acquisition, Formal analysis, Data curation, Conceptualization. **Jesús López-Sánchez:** Writing – review & editing, Writing – original draft, Visualization, Validation, Supervision, Resources, Project administration, Methodology, Investigation, Funding acquisition, Formal analysis, Data curation, Conceptualization. **Alberto Castellano-Soria:** Writing – review & editing, Formal analysis, Data curation. **Rosalía López-Méndez:** Writing – review & editing, Resources, Formal analysis, Data curation. **Carmen del Pino-Batlles:** Writing – review & editing, Writing – original draft, Visualization, Investigation, Formal analysis, Data curation, Conceptualization. **Aída Serrano:** Writing – review & editing, Writing – original draft, Resources, Investigation, Formal analysis, Data curation, Conceptualization.

Declaration of Competing Interest

The authors declare that they have no known competing financial interests or personal relationships that could have appeared to influence the work reported in this paper.

Data availability

Data will be made available on request.

Acknowledgements

This work has received funding from the Comunidad de Madrid through the project S2018/NMT-4321 NANOMAGCOST and from Ministerio de Ciencia e Innovación (MICNN) through PID2021-126323OA-100 and PDC2022-133039-I00. We thank the CLAESS beamline staff for their support during the experiments. A. E. acknowledges the financial support from MICINN (PID2021-127033OB-C21) and Comunidad de Madrid (2018-T1/IND-1005 project). R.L.-M. acknowledges FPI PRE2020-96246 grant under the Severo Ochoa program (CEX2020-001039-S) at IMDEA Nanociencia. A.S. acknowledges

financial support from PID2021-124585NB-C33 funded by MCIN/AEI/10.13039/501100011033 and by "ERDF A way of making Europe'', by Project TED2021-130957B-C51 funded by MCIN/AEI/10.13039/501100011033 and by the "European Union NextGenerationEU/PRTR'' and from grant RYC2021-031236-I funded by MCIN/AEI/10.13039/501100011033 and by the "European Union NextGenerationEU/PRTR". J.L.-S. acknowledges financial support from Spanish Ministry of Economic Affairs and Digital Transformation (MINECO) through the project PID2021-122980OB-C51 and from grant RYC2022-035912-I funded by MCIU/AEI/10.13039/501100011033 and by the European Social Fund Plus (ESF+).

References

[1] Z. Guo, J. Yin, Y. Bai, D. Zhu, K. Shi, G. Wang, K. Cao, W. Zhao, Spintronics for energy- efficient computing: an overview and outlook, Proc. IEEE 109 (2021) 1398–1417, https://doi.org/10.1109/JPROC.2021.3084997.

[2] G. Patel, F. Ganss, R. Salikhov, S. Stienen, L. Fallarino, R. Ehrler, R.A. Gallardo, O. Hellwig, K. Lenz, J. Lindner, Structural and magnetic properties of thin cobalt films with mixed hcp and fcc phases, Phys. Rev. B 108 (2023) 184429, https://doi.org/10.1103/PhysRevB.108.184429.

[3] V.F. Puntes, K.M. Krishnan, A.P. Alivisatos, Colloidal nanocrystal shape and size control: the case of cobalt, Science 291 (2001) 2115–2117, https://doi.org/10.1126/science.1058495.

[4] F. Dumestre, B. Chaudret, C. Amiens, M.C. Fromen, M.J. Casanove, P. Renaud, P. Zurcher, Shape control of thermodynamically stable cobalt nanorods through organometallic chemistry, Angew. Chem. Int. 41 (2002) 4286–4289, https://doi.org/10.1002/1521-3773(20021115)41:22<4286::AID-ANIE4286>3.0.CO;2-M.

[5] Y. Liu, X. Yan, Y. Tang, N. Lu, T. Zhang, Z. Xu, Y. Xing, P. Zhao, M. Liu, Y. Zhu, Z. Zhang, M. Yang, Cobalt nanoparticles decorated bamboo-like N-doped carbon nanotube as nanozyme sensor for efficient biosensing, J. Electroanal. Chem. 926 (2022) 116932, https://doi.org/10.1016/j.jelechem.2022.116932.

[6] S.M. Ansari, R.D. Bhor, K.R. Pai, D. Sen, S. Mazumder, K. Ghosh, Y.D. Kolekar, C. V. Ramana, Cobalt nanoparticles for biomedical applications: Facile synthesis, physiochemical characterization, cytotoxicity behavior and biocompatibility, Appl. Surf. Sci. 414 (2017) 171–187, https://doi.org/10.1016/j.apsusc.2017.03.002.

[7] Y. Fang, Y. Yao, H. Yang, Y. Fan, N. Nomura, W. Zhou, D. Ni, X. Li, W. Jiang, P. Qiu, W. Luo, Incorporating cobalt nanoparticles in nitrogen-doped mesoporous carbon spheres through composite micelle assembly for high-performance lithium-sulfur batteries, ACS Appl. Mater. Interfaces 13 (2021) 38604–38612, https://doi.org/10.1021/acsami.1c10227.

[8] B. Lu, Y.M. Li, S.F. Liu, Q. Sun, Cobalt nanoparticles inlayed N-doped mesoporous carbon microspheres for high performance lithium-selenium battery, J. Electroanal. Chem. 947 (2023) 117799, https://doi.org/10.1016/j.jelechem.2023.117799.

[9] A.K. Beheshti, M. Rezaei, S.M. Alavi, E. Akbari, M. Varbar, Cobalt nanoparticle synthesis through the mechanochemical and chemical reduction method as a highly active and reusable catalyst for H_2 production via sodium borohydride hydrolysis process, Int. J. Hydrog. Energy 51 (2024) 661–670, https://doi.org/10.1016/j.ijhydene.2023.10.168.

[10] H. Fei, Y. Yang, Z. Peng, G. Ruan, Q. Zhong, L. Li, E.L.G. Samuel, J.M. Tour, Cobalt nanoparticles embedded in nitrogen-doped carbon for the hydrogen evolution reaction, ACS Appl. Mater. Interfaces 7 (2015) 8083–8087, https://doi.org/10.1021/acsami.5b00652.

[11] H. Liu, Y. Li, M. Yuan, G. Sun, H. Li, S. Ma, Q. Liao, Y. Zhang, In situ preparation of cobalt nanoparticles decorated in n-doped carbon nanofibers as excellent electromagnetic wave absorbers, ACS Appl. Mater. Interfaces 10 (2018) 22591–22601, https://doi.org/10.1021/acsami.8b05211.

[12] E. Camilli, A.F. Pighin, G.J. Copello, M.E. Villanueva, Cobalt/carbon quantum dots core-shell nanoparticles as an improved catalyst for Fenton-like reaction, Nano Struct. Nano Objects 37 (2024) 101097, https://doi.org/10.1016/j.nanoso.2024.101097.

[13] M. Liu, J. Liu, Z. Li, F. Wang, Atomic-level Co_3O_4 layer stabilized by metallic cobalt nanoparticles: a highly active and stable electrocatalyst for oxygen reduction, ACS Appl. Mater. Interfaces 10 (2018) 7052–7060, https://doi.org/10.1021/acsami.7b16549.

[14] T. Zhang, Y. Zhao, F. Liu, M. Zheng, K. Shi, J. Liu, Y. Sun, Y. Zhang, H. Wang, Novel cobalt nanorods@ cobalt-platinum nanoparticles for electrocatalytic hydrogen evolution reactions and oxygen evolution reactions study, Int J. Hydrog. Energy 58 (2024) 646–656, https://doi.org/10.1016/j.ijhydene.2024.01.171.

[15] A. Chaturvedi, P.P. Kundu, Co-doped zeolite-GO nanocomposite as a high-performance ORR catalyst for sustainable bioelectricity generation in air-cathode single-chambered microbial fuel cells, ACS Appl. Mater. Interfaces (2022) 33219–33233, https://doi.org/10.1021/acsami.2c07638.

[16] T. Senthamarai, V.G. Chandrashekhar, M.B. Gawande, N.V. Kalevaru, R. Zbořil, P. C.J. Kamer, R.V. Jagadeesh, M. Beller, Ultra-small cobalt nanoparticles from molecularly-defined Co-salen complexes for catalytic synthesis of amines, Chem. Sci. 11 (2020) 2973–2981, https://doi.org/10.1039/c9sc04963k.

[17] L.G. Jacobsohn, M.E. Hawley, D.W. Cooke, M.F. Hundley, J.D. Thompson, R. K. Schulze, M. Nastasi, Synthesis of cobalt nanoparticles by ion implantation and effects of postimplantation annealing, J. Appl. Phys. 96 (2004) 4444–4450, https://doi.org/10.1063/1.1787143.

[18] J. Ahmed, S. Sharma, K.V. Ramanujachary, S.E. Lofland, A.K. Ganguli, Microemulsion-mediated synthesis of cobalt (pure fcc and hexagonal phases) and cobalt-nickel alloy nanoparticles, J. Colloid Interface Sci. 336 (2009) 814–819, https://doi.org/10.1016/j.jcis.2009.04.062.

[19] A. Bake, M. Rezoanur Rahman, P.J. Evans, M. Cortie, M. Nancarrow, R. Abrudan, F. Radu, Y. Khaydukov, G. Causer, S. Callori, K.L. Livesey, D. Mitchell, Z. Pastuovic, X. Wang, D. Cortie, Structure and magnetism of ultra-small cobalt particles assembled at titania surfaces by ion beam synthesis, Appl. Surf. Sci. 570 (2021) 151068, https://doi.org/10.1016/j.apsusc.2021.151068.

[20] M. Ştefănescu, T. Dippong, M. Stoia, O. Ştefănescu, Study on the obtaining of cobalt oxides by thermal decomposition of some complex combinations, undispersed and dispersed in SiO_2 matrix, J. Therm. Anal. Calorim. 94 (2008) 389–393, https://doi.org/10.1007/s10973-008-9111-2.

[21] T. Dippong, E.A. Levei, C. Leostean, O. Cadar, Impact of annealing temperature and ferrite content embedded in SiO_2 matrix on the structure, morphology and magnetic characteristics of $(Co_{0.4}Mn_{0.6}Fe_2O_4)_\delta$ $(SiO_2)_{100-\delta}$ nanocomposites, J. Alloy. Compd. 868 (2021) 159203, https://doi.org/10.1016/j.jallcom.2021.159203.

[22] F. Tang, L. Li, D. Chen, Mesoporous silica nanoparticles: synthesis, biocompatibility and drug delivery, Adv. Mater. 24 (2012) 1504–1534, https://doi.org/10.1002/adma.201104763.

[23] I.L. Medintz, H.T. Uyeda, E.R. Goldman, H. Mattoussi, Quantum dot bioconjugates for imaging, labelling and sensing, Nat. Mater. 4 (2005) 435–446, https://doi.org/10.1038/nmat1390.

[24] W. Zhao, Q. Shen, T. Nan, M. Zhou, Y. Xia, G. Hu, Q. Zheng, Y. Wu, T. Bian, T. Wei, C. Zhang, Cobalt-based catalysts for heterogeneous peroxymonosulfate (PMS) activation in degradation of organic contaminants: recent advances and perspectives, J. Alloy. Compd. 958 (2023) 170370, https://doi.org/10.1016/j.jallcom.2023.170370.

[25] H. Zhang, C. Liang, J. Liu, Z. Tian, G. Shao, The formation of onion-like carbon-encapsulated cobalt carbide core/shell nanoparticles by the laser ablation of metallic cobalt in acetone, Carbon 55 (2013) 108–115, https://doi.org/10.1016/j.carbon.2012.12.015.

[26] Y. Huang, W. Zhang, Magnetic nanoparticle-supported organocatalysis, Green. Process. Synth. 2 (2013) 603–609, https://doi.org/10.1515/gps-2013-0076.

[27] S. Mourdikoudis, A. Kostopoulou, A.P. LaGrow, Magnetic nanoparticle composites: synergistic effects and applications, Adv. Sci. (2021) 1–57, https://doi.org/10.1002/advs.202004951.

[28] D. Matatagui, J. López-Sánchez, A. Peña, A. Serrano, A. del Campo, O.Rodríguez de la Fuente, N. Carmona, E. Navarro, P. Marín, M. del Carmen Horrillo, Ultrasensitive NO_2 gas sensor with insignificant NH_3-interference based on a few-layered mesoporous graphene, Sens. Actuators B Chem. 335 (2021) 129657, https://doi.org/10.1016/j.snb.2021.129657.

[29] J. López-Sánchez, Á. Peña, A. Serrano, A. del Campo, Ó. Rodríguez de la Fuente, N. Carmona, D. Matatagui, M.D.C. Horrillo, J. Rubio-Zuazo, E. Navarro, P. Marín, Generation of defective few-layered graphene mesostructures by high-energy ball milling and their combination with FeSiCuNbB microwires for reinforcing microwave absorbing properties, ACS Appl. Mater. Interfaces 15 (2023) 3507–3521, https://doi.org/10.1021/acsami.2c19886.

[30] S. Wu, X. Qu, J. Zhu, X. Liu, H. Mao, K. Wang, G. Zhou, J. Chi, L. Wang, Recent advances in metal-organic frameworks derived electrocatalysts for oxygen reduction reaction, J. Alloy. Compd. 970 (2024) 172518, https://doi.org/10.1016/j.jallcom.2023.172518.

[31] J. Yu, G. Chen, J. Sunarso, Y. Zhu, R. Ran, Z. Zhu, W. Zhou, Z. Shao, Cobalt oxide and cobalt-graphitic carbon core shell based catalysts with remarkably high oxygen reduction reaction activity, Adv. Sci. 3 (2016) 1600060, https://doi.org/10.1002/advs.201600060.

[32] S. Shin, Y. Yoon, S. Park, M.W. Shin, Fabrication of core-shell structured cobalt nanoparticle/carbon nanofiber as a bifunctional catalyst for the oxygen reduction/evolution reactions, J. Alloy. Compd. 939 (2023) 168731, https://doi.org/10.1016/j.jallcom.2023.168731.

[33] J. Zhao, X. Quan, S. Chen, Y. Liu, H. Yu, Cobalt nanoparticles encapsulated in porous carbons derived from core-shell zif67@zif8 as efficient electrocatalysts for oxygen evolution reaction, ACS Appl. Mater. Interfaces 9 (2017) 28685–28694, https://doi.org/10.1021/acsami.7b10138.

[34] X. Yan, C.-L. Dong, Y.-C. Huang, Y. Jia, L. Zhang, S. Shen, J. Chen, X. Yao, Probing the active sites of carbon-encapsulated cobalt nanoparticles for oxygen reduction, Small Methods 3 (2019) 1800439, https://doi.org/10.1002/smtd.201800439.

[35] B. Chen, S. Chen, H.A. Bandal, R. Appiah-Ntiamoah, A.R. Jadhav, H. Kim, Cobalt nanoparticles supported on magnetic core-shell structured carbon as a highly efficient catalyst for hydrogen generation from $NaBH_4$ hydrolysis, Int. J. Hydrog. Energy 43 (2018) 9296–9306, https://doi.org/10.1016/j.ijhydene.2018.03.193.

[36] Y. Liu, B. Hou, C. Chen, L. Jia, Z. Ma, Q. Wang, D. Li, Carbon coated cobalt catalysts for direct synthesis of middle n-alkanes from syngas, Fuel 327 (2022) 124889, https://doi.org/10.1016/j.fuel.2022.124889.

[37] C. Yu, J.S. Qiu, Preparation and magnetic behavior of carbon-encapsulated cobalt and nickel nanoparticles from starch, Chem. Eng. Res. Des. 86 (2008) 904–908, https://doi.org/10.1016/j.cherd.2008.02.006.

[38] R. Kuchi, M. Sharma, S.W. Lee, D. Kim, N. Jung, J.R. Jeong, Rational design of carbon shell-encapsulated cobalt nanospheres to enhance microwave absorption performance, Prog. Nat. Sci. Mater. Int. 29 (2019) 88–93, https://doi.org/10.1016/j.pnsc.2019.03.013.

[39] A. Kotoulas, C. Dendrinou-Samara, C. Sarafidis, T. Kehagias, J. Arvanitidis, G. Vourlias, M. Angelakeris, O. Kalogirou, Carbon-encapsulated cobalt nanoparticles: synthesis, properties, and magnetic particle hyperthermia

efficiency, J. Nanopart. Res. 19 (2017) 399, https://doi.org/10.1007/s11051-017-4099-9.
[40] J. López-Sánchez, A. Muñoz-Noval, C. Castellano, A. Serrano, A. del Campo, M. Cabero, M. Varela, M. Abuín, J. de la Figuera, J.F. Marco, G.R. Castro, O. Rodríguez de la Fuente, N. Carmona, Origin of the magnetic transition at 100 K in ε-Fe_2O_3 nanoparticles studied by x-ray absorption fine structure spectroscopy, J. Condens. Matter Phys. 29 (2017) 485701, https://doi.org/10.1088/1361-648X/aa904b.
[41] J. López-Sánchez, A. Serrano, A. del Campo, Á. Muñoz-Noval, E. Salas-Colera, M. Cabero, M. Varela, M. Abuín, G.R. Castro, J. Rubio-Zuazo, Ó. Rodríguez de la Fuente, N. Carmona, A combined micro-Raman, x-ray absorption and magnetic study to follow the glycerol-assisted growth of epsilon-iron oxide sol-gel coatings, J. Alloy. Compd. 892 (2022) 162061, https://doi.org/10.1016/j.jallcom.2021.162061.
[42] T. Dippong, E.A. Levei, F. Goga, O. Cadar, Influence of Mn^{2+} substitution with Co^{2+} on structural, morphological and coloristic properties of $MnFe_2O_4/SiO_2$ nanocomposites, Mater. Charact. 172 (2021) 110835, https://doi.org/10.1016/j.matchar.2020.110835.
[43] M. Stoia, M. Stefanescu, T. Dippong, O. Stefanescu, P. Barvinschi, Low temperature synthesis of Co_2SiO_4/SiO_2 nanocomposite using a modified sol–gel method, J. Sol. Gel Sci. Technol. 54 (2010) 49–56, https://doi.org/10.1007/s10971-010-2156-2.
[44] T. Jaumann, E.M.M. Ibrahim, S. Hampel, D. Maier, A. Leonhardt, B. Büchner, The synthesis of superparamagnetic cobalt nanoparticles encapsulated in carbon through high-pressure CVD, Chem. Vap. Depos. 19 (2013) 228–234, https://doi.org/10.1002/cvde.201207020.
[45] G. Sun, X. Li, Y. Zhang, X. Wang, D. Jiang, F. Mo, A simple detonation technique to synthesize carbon-coated cobalt, J. Alloy. Compd. 473 (2009) 212–214, https://doi.org/10.1016/j.jallcom.2008.05.034.
[46] B.M. Sperry, N.A. Kukhta, Y. Huang, C.K. Luscombe, Ligand decomposition during nanoparticle synthesis: influence of ligand structure and precursor selection, Chem. Mater. 35 (2023) 570–583, https://doi.org/10.1021/acs.chemmater.2c03006.
[47] A. Castellano-Soria, J. López-Sánchez, C. Granados-Miralles, M. Varela, E. Navarro, C. González, P. Marín, Novel one-pot sol-gel synthesis route of Fe_3C/few-layered graphene core/shell nanoparticles embedded in a carbon matrix, J. Alloy. Compd. 902 (2022) 163662, https://doi.org/10.1016/j.jallcom.2022.163662.
[48] S. Mourdikoudis, M. Menelaou, N. Fiuza-Maneiro, G. Zheng, S. Wei, J. Pérez-Juste, L. Polavarapu, Z. Sofer, Oleic acid/oleylamine ligand pair: A versatile combination in the synthesis of colloidal nanoparticles, Nanoscale Horiz. 7 (2022) 941–1015, https://doi.org/10.1039/D2NH00111J.
[49] S.F. Shaikh, R.S. Mane, B.K. Min, Y.J. Hwang, O. Joo, D-sorbitol-induced phase control of TiO_2 nanoparticles and its application for dye-sensitized solar cells, Sci. Rep. 6 (2016) 20103, https://doi.org/10.1038/srep20103.
[50] Z. Schnepp, S.C. Wimbush, M. Antonietti, C. Giordano, Synthesis of highly magnetic iron carbide nanoparticles via a biopolymer route, Chem. Mater. 22 (2010) 5340–5344, https://doi.org/10.1021/cm101746z.
[51] G.W. Gokel, DeanS Handbook of Organic Chemistry, 2nd ed., McGraw-Hill Education, 2004.
[52] F.L. Winter, P. Diehl, P. Telaar, C.M. Watermann, S. Kaluza, M. Muhler, U.-P. Apfel, B. Zeidler-Fandrich, Influence of the catalyst precursor for cobalt on activated carbon applied in ammonia decomposition, Catal. Today 429 (2024) 114502, https://doi.org/10.1016/j.cattod.2023.114502.
[53] N. Doebelin, R. Kleeberg, Profex: a graphical user interface for the Rietveld refinement program BGMN, J. Appl. Crystallogr. 48 (2015) 1573–1580, https://doi.org/10.1107/S1600576715014685.
[54] L. Simonelli, C. Marini, W. Olszewski, M. Ávila Pérez, N. Ramanan, G. Guilera, V. Cuartero, K. Klementiev, CLÆSS: the hard x-ray absorption beamline of the ALBA CELLS synchrotron, Cogent, Phys 3 (2016) 1231987, https://doi.org/10.1080/23311940.2016.1231987.
[55] B. Ravel, M. Newville, ATHENA, ARTEMIS, HEPHAESTUS: data analysis for x-ray absorption spectroscopy using IFEFFIT, J. Synchrotron Radiat. 12 (2005) 537–541, https://doi.org/10.1107/S0909049505012719.
[56] M. Newville, B. Ravel, D. Haskel, J.J. Rehr, E.A. Stern, Y. Yacoby, Analysis of multiple-scattering XAFS data using theoretical standards, Phys. B Condens. Matter 208–209 (1995) 154–156, https://doi.org/10.1016/0921-4526(94)00655-F.
[57] T.S. Ong, H. Yang, Effect of atmosphere on the mechanical milling of natural graphite, Carbon 38 (2000) 2077–2085, https://doi.org/10.1016/S0008-6223(00)00064-6.
[58] M. El-Tahawy, L. Péter, L.F. Kiss, J. Gubicza, Z. Czigány, G. Molnár, I. Bakonyi, Anisotropic magnetoresistance (AMR) of cobalt: hcp-Co vs. fcc-Co, J. Magn. Magn. Mater. 560 (2022) 169660, https://doi.org/10.1016/j.jmmm.2022.169660.
[59] S.S. Kalyan Kamal, P.K. Sahoo, M. Premkumar, N.V. Rama Rao, T. Jagadeesh Kumar, B. Sreedhar, A.K. Singh, S. Ram, K. Chandra Sekhar, Synthesis of cobalt nanoparticles by a modified polyol process using cobalt hydrazine complex, J. Alloy. Compd. 474 (2009) 214–218, https://doi.org/10.1016/j.jallcom.2008.06.160.
[60] ASM International, Binary Alloy Phase Diagrams, Second, ASM International, [Materials Park, Ohio], Ohio, 1996.
[61] A. Castellano-Soria, J. López-Sánchez, A. Serrano, G. Gorni, M. Varela, I. Sardinero, N. Carmona, A. Hernando, P. Marín, E. Navarro, Sol-gel synthesis control of iron-cobalt alloy/ferrite core/shell nanoparticles supported by a carbon medium with semi-hard magnetic features, J. Alloy. Compd. 959 (2023) 170244, https://doi.org/10.1016/j.jallcom.2023.170244.
[62] T. Bredow, A.R. Gerson, Effect of exchange and correlation on bulk properties of MgO, NiO, and CoO, Phys. Rev. B 61 (2000) 5194, https://doi.org/10.1103/PhysRevB.61.5194.
[63] P.A. Stampe, R.J. Kennedy, Y. Xin, J.S. Parker, Investigation of the cobalt distribution in TiO_2:Co thin films, J. Appl. Phys. 92 (2002) 7114–7121, https://doi.org/10.1063/1.1521259.
[64] L. Chen, T. Mashimo, C. Iwamoto, H. Okudera, E. Omurzak, H.S. Ganapathy, H. Ihara, J. Zhang, Z. Abdullaeva, S. Takebe, A. Yoshiasa, Synthesis of novel CoCx@C nanoparticles, Nanotechnology 24 (2013) 045602, https://doi.org/10.1088/0957-4484/24/4/045602.
[65] T. Yamamoto, Assignment of pre-edge peaks in K-edge x-ray absorption spectra of 3d transition metal compounds: electric dipole or quadrupole? X-Ray Spectrom. 37 (2008) 572–584, https://doi.org/10.1002/xrs.1103.
[66] M. Abuín, A. Serrano, J. Chaboy, M.A. García, N. Carmona, XAS study of Mn, Fe and Cu as indicators of historical glass decay, J. Anal. . Spectrom. 28 (2013) 1118–1124, https://doi.org/10.1039/c3ja30374h.
[67] V. Kunzl, A linear dependence of energy levels on the valency of elements, Collect. Czech. Chem. Commun. 4 (1932) 213–224, https://doi.org/10.1135/cccc19320213.
[68] D.J. Sprouster, M.C. Ridgway, Ion beam formation and modification of cobalt nanoparticles, Appl. Sci. 2 (2012) 396–442, https://doi.org/10.3390/app2020396.
[69] K.R. Kittilstved, D.A. Schwartz, A.C. Tuan, S.M. Heald, S.A. Chambers, D. R. Gamelin, Direct kinetic correlation of carriers and ferromagnetism in Co^{2+}:ZnO, Phys. Rev. Lett. 97 (2006) 037203, https://doi.org/10.1103/PhysRevLett.97.037203.
[70] F. De Groot, G. Vankó, P. Glatzel, The 1s x-ray absorption pre-edge structures in transition metal oxides, J. Condens. Matter Phys. 21 (2009) 104207, https://doi.org/10.1088/0953-8984/21/10/104207.
[71] J. Necib, J. López Sánchez, F. Rubio-Marcos, A. Serrano, E. Navarro, Á. Peña, T. Mnasri, M. Smari, R.E. Rojas-Hernandez, N. Carmona, P. Marín, A feasible pathway to stabilize the monoclinic and tetragonal phase coexistence in barium titanate-based ceramics, J. Mater. Chem. C (2022) 17743–17756, https://doi.org/10.1039/d2tc04265g.
[72] J. Jiang, W. Feng, Y. Wen, L. Yin, H. Wang, X. Feng, Y. li Pei, R. Cheng, J. He, Tuning 2D magnetism in cobalt monoxide nanosheets via in situ nickel-doping, Adv. Mater. 35 (2023) 2301668, https://doi.org/10.1002/adma.202301668.
[73] S.B. Qadri, S.D. Johnson, S.N. Qadri, E.P. Gorzkowski, B.B. Rath, K. Bussmann, Magnetic properties of metastable bcc-cobalt during reduction of cobalt oxide (Co_3O_4), J. Electron. Mater. 48 (2019) 7882–7887, https://doi.org/10.1007/s11664-019-07627-3.
[74] H. Shao, Y. Huang, H.S. Lee, Y.J. Suh, C.O. Kim, Effect of PVP on the morphology of cobalt nanoparticles prepared by thermal decomposition of cobalt acetate, Curr. Appl. Phys. 6 (2006) e195–e197, https://doi.org/10.1016/j.cap.2006.01.038.
[75] J. López-Sánchez, A. Muñoz-Noval, A. Serrano, M. Abuín, J. De La Figuera, J. F. Marco, L. Pérez, N. Carmona, O. Rodríguez de la Fuente, Growth, structure and magnetism of ε-Fe_2O_3 in nanoparticle form, RSC Adv. 6 (2016) 46380–46387, https://doi.org/10.1039/c6ra01912a.
[76] A. Longo, X.L. Wang, A. Ruotolo, A. Peluso, G. Carotenuto, R. Lortz, Effect of the polymeric matrix on the structural and magnetic properties of hematite/polymer composites, J. Nanopart. Res. 14 (2012) 1314, https://doi.org/10.1007/s11051-012-1314-6.